energies

MDPI

Review

Stannous Tungstate Semiconductor for Photocatalytic Degradation and Photoelectrochemical Water Splitting: A Review

Weixin Qiu and Yang Liu *

School of Chemistry and Chemical Engineering, Central South University, Changsha 410083, China
* Correspondence: yangliu_csu@csu.edu.cn

Abstract: The use of photocatalysis and photoelectrocatalysis is expected to achieve the efficient utilization of solar energy to alleviate and even solve the problems of energy depletion and environmental pfollution. At present, stannous tungstate materials have attracted extensive attention in the fields of photocatalysis and photoelectrocatalysis as favorable candidates for such utilization because of their narrow band gap energy (which is~1.7 eV for the α phase and ~2.7 eV for the β phase, respectively) and unique band structure (which covers the oxidation and reduction potential of water). However, their practical application is still limited by excessive electron–hole recombination and poor stability. In this review, basic information (crystal and electronic structures) related to photocatalysis and photoelectrocatalysis is presented. Additionally, various strategies to enhance the photocatalytic and photoelectrochemical properties of stannous tungstate materials, such as morphological modification, crystal facet engineering, doping modification, and multicomponent compositing, are summarized. Furthermore, the achievements and difficulties of the relevant studies are discussed. The information presented in this review can provide a reference for subsequent research on the photocatalytic and photoelectrochemical performance of tungstate-based materials.

Keywords: stannous tungstate; photocatalysis; photoelectrocatalysis; water splitting; degradation

Citation: Qiu, W.; Liu, Y. Stannous Tungstate Semiconductor for Photocatalytic Degradation and Photoelectrochemical Water Splitting: A Review. *Energies* **2022**, *15*, 9194. https://doi.org/10.3390/en15239194

Academic Editor: Andrea Reverberi

Received: 23 October 2022
Accepted: 1 December 2022
Published: 4 December 2022

Publisher's Note: MDPI stays neutral with regard to jurisdictional claims in published maps and institutional affiliations.

Copyright: © 2022 by the authors. Licensee MDPI, Basel, Switzerland. This article is an open access article distributed under the terms and conditions of the Creative Commons Attribution (CC BY) license (https://creativecommons.org/licenses/by/4.0/).

1. Introduction

With the rapid development of technology, energy has become a necessity for social operation, and the human consumption of non-renewable traditional energy (from sources such as oil and coal) is decreasing. The energy crisis has become an urgent problem that needs to be solved. Therefore, researchers are enthusiastically looking for alternative renewable clean energy sources. Among the many potential energy sources, solar energy has attracted significant attention due to its large reserves and reproducibility. Although solar energy exhibits a variety of excellent properties, its dispersion, instability and intermittency have led to its low utilization. Therefore, exploring efficient ways to better use solar energy is necessary for the generation of alternative power. Photocatalytic and photoelectrochemical methods show promise for degrading pollutants and generating new kinds of energy (such as hydrogen and chemical) via the use of solar energy. All the relevant reactions are completed by the photo-generated holes and electrons; thus, they follow a similar principle. Since the first report of TiO_2 in 1972 [1], different kinds of materials with a smaller band gap than that of TiO_2 (3.0–3.2 eV) have been explored [2].

One of these materials is stannous tungstate ($SnWO_4$), which is a potential catalyst due to its narrow band gap, suitable band position, and nontoxicity [3]. However, due to its low charge separation efficiency and poor stability [4], its photocatalytic and photoelectrochemical performance has not met theoretical expectations. To solve this problem, many researchers are committed to obtaining a better catalytic performance and higher

solar energy efficiency by means of morphology control, doping, and multi-component compositing. In this paper, we describe the synthesis method, physical characteristics, and activities regarding the photocatalysis and photoelectrocatalysis of stannous tungstate. In addition, the challenges and future outlook regarding the use of stannous tungstate in photoelectrochemical water splitting are summarized.

2. Structure, Properties, and Synthesis of $SnWO_4$

In the 1970s, Jeitschko and Sleight reported the crystalline structure and morphology of the low-temperature (α) and high-temperature (β) phases of stannous tungstate materials [5, 6]. Orthorhombic α–$SnWO_4$(Figure 1a) exhibits a stable structure below 670 °C, and it tends to transform into cubic β–$SnWO_4$ (Figure 1b) above 670 °C [7]. A reverse transition from the β–phase to the α–phase may occur under negative pressure, and the W is replaced by Mo [8]. In the crystal of α–$SnWO_4$, W and O form WO_6 octahedral structures that are interconnected in four corners, while O binds to Sn in a regular octahedral form [5]. For β–$SnWO_4$, the W atoms of β– form WO_4^{2-} tetrahedrons with O and disperse within the crystal, whereas near the Sn atoms, O is bound to it as a twisted octahedron [6].

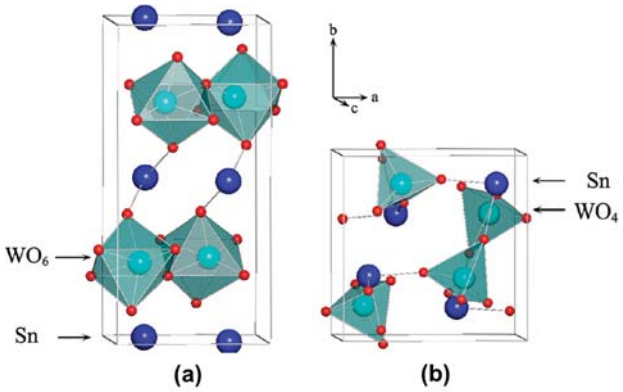

Figure 1. Crystal structures of $SnWO_4$ polymorphs: (**a**) α–$SnWO_4$ (orthorhombic); (**b**) β–$SnWO_4$ (cubic)..

This difference in structure leads to different properties for the α and β phases. The W–O bond in the WO_4^{2-} tetrahedron (~1.75 Å) [5] is shorter than that in the WO_6 octahedrons (~1.80–2.15 Å) [6]. It leads to a larger crystal field-splitting energy and a higher orbital energy of W in β–$SnWO_4$. The conduction band edge of the α phase is mainly composed of a W 5d orbital, while the β phase contains an Sn 5p orbital, in addition to the W 5d orbital (Figure 2). The valence bands of both $SnWO_4$ are formed by hybridizing the O 2p and Sn 5s orbitals, and the Sn–O bonds are almost identical in length (~2.20–2.80 Å) [5, 6]. Thus, the positions of the valence bands are similar. These characteristics result in a narrower band gap for α–$SnWO_4$ (~1.7 eV) than for β–$SnWO_4$ (~2.7 eV) [3], and α–$SnWO_4$ has a wider range of light absorption and a higher theoretical photocurrent density (~17 $mA \cdot cm^{-2}$ [9]) than β–$SnWO_4$. In addition, the β phase is a direct band gap and the α phase is an indirect band gap [3], which leads to a higher carrier separation efficiency for the α phase than the β phase [10]. Due to the wider band gap, the photo-generated electrons (holes) of β–$SnWO_4$ show a more significant reduction (oxidation) activity. Thus, β–$SnWO_4$ was used in photocatalysis, and only α–$SnWO_4$ has been used in photoelectrochemical water splitting and sulfite oxidation. However, in addition to the excellent optical properties mentioned above, the use of stannous tungstate exhibits problems that urgently need to be solved. Since Sn is divalent and oxidizable in $SnWO_4$, it is susceptible to photocorrosion, which is attributed to stannous, and the following reaction occurs: $SnWO_4 + H_2O + 2h^+ \rightarrow SnO_2 + WO_3 + 2H^+$. Therefore, $SnWO_4$ has poor stability, which limits its performance in practical applications [4]. At the same time, a recombination of carriers occurs in the diffusion process of $SnWO_4$. Its diffusion length is short, which limits the

number of photo-generated carriers that can arrive at the surface of the crystal, leading to unsatisfactory photocatalytic and photoelectrochemical performance.

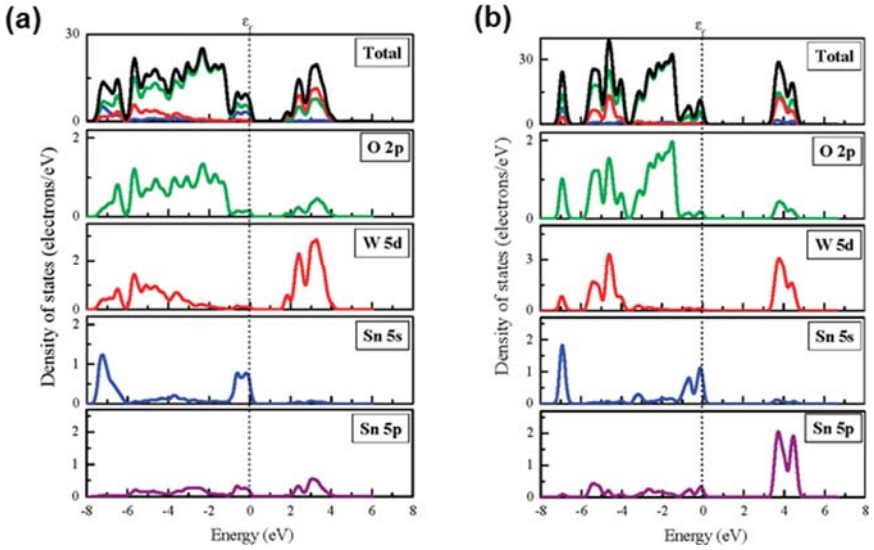

Figure 2. Partial density states of α−$SnWO_4$ (**a**) and β−$SnWO_4$ (**b**) [3].

Various methods have been developed to synthesize $SnWO_4$ materials, and their differences in thermodynamic stability lead to changes in the synthesis of α−$SnWO_4$ and β−$SnWO_4$. Because the α phase is a kind of crystalline phase at low temperatures, its synthesis conditions are milder. Many methods can be used to synthesize the α phase, e.g., hydrothermal methods, solid–solid reaction methods [3, 11-13], and magnetron sputtering methods [10, 14, 15]. Each synthesis method has its own advantages. The hydrothermal method can be used to obtain crystals with a complete crystal phase, small particle size, and uniform distribution. A magnetron sputtering method can obtain dense and uniform high-quality thin films. The solid–solid reaction method possesses a simple process and a large output. However, the synthesis of the high-temperature crystalline β−phase is relatively harsh because it requires higher temperature conditions (which should be obtained by rapid cooling at more than 940 K). It has been reported that most β−$SnWO_4$ powders are synthesized with a high-temperature solid phase method[11, 12, 16, 17]. β−$SnWO_4$ can also be obtained by using $NaWO_4$ as a raw material through kinetic control under more mild conditions [18]. Jan Ungelenk and Claus Feldmann synthesized β−$SnWO_4$ using a microemulsion method at low temperatures [19]. When W and O combine to form a discrete WO_4^{2-} tetrahedron in $NaWO_4$, the structure is similar to that of β−$SnWO_4$, so Na_2WO_4 is likely to be directly converted to β−$SnWO_4$. Additionally, assisted by hydrothermal [20, 21] and microwave-assisted hydrothermal methods [22], α−$SnWO_4$ can also be synthesized using $NaWO_4$ and $SnCl_2$ as the precursors.

To synthesize the film for photoelectrochemical water spliting, an indirect or direct coating method can be used. In indirect coating, as-prepared $SnWO_4$ powders are drop-cast onto conductive substrates. This is an easy-to-perform method, but the performance of the photoanode is weak due to the poor charge transfer caused by bad connections between the particles. For direct coating, Moritz Kölbach et al. employed a pulsed laser-deposited method that used an α−$SnWO_4$ target formed by annealing WO_3 (99.99%) and SnO (99.99%) powders [23]. Bozheyev et al. reported on the use of a magnetron co-sputtering method in which Sn (99.99%) and W (99.95%) were the targets, and the deposition was performed with the existence of O_2 [24]. Recently, Gottesman used a new method—rapid thermal processing—to synthesize an α−$SnWO_4$ film. The technique could be used to treat a sample at higher temperatures, without destroying the glass-based F:SnO_2 (FTO), and a desired crystallinity with few defects was obtained [25]. Liu et al. used a

chemical vapor deposition to convert WO_3 into α–$SnWO_4$, and the reaction is shown in Equation (1) [26]. An in situ hydrothermal conversion method was also reported, in which WO_3 was used as a precursor to react with Sn^{2+} in the solution [27]. The possible reactions occurring in this method are illustrated as Equations (2)–(3) [28]. As a result, the α–$SnWO_4$ film exhibits similar nanostructured array morphology to that of WO_3 films due to the inherited behavior (Figure 3) [28]. The anion in hydrothermal conversion solutions may also affect the morphology of α–$SnWO_4$ films [29].

$$4WO_3 + 3SnCl_2 \rightleftharpoons 3SnWO_4 + WCl_6 \quad (1)$$

$$WO_3 + H_2O \rightleftharpoons 2H^+ + WO_4^{2-} \quad (2)$$

$$WO_4^{2-} + Sn^{2+} \rightleftharpoons SnWO_4 \quad (3)$$

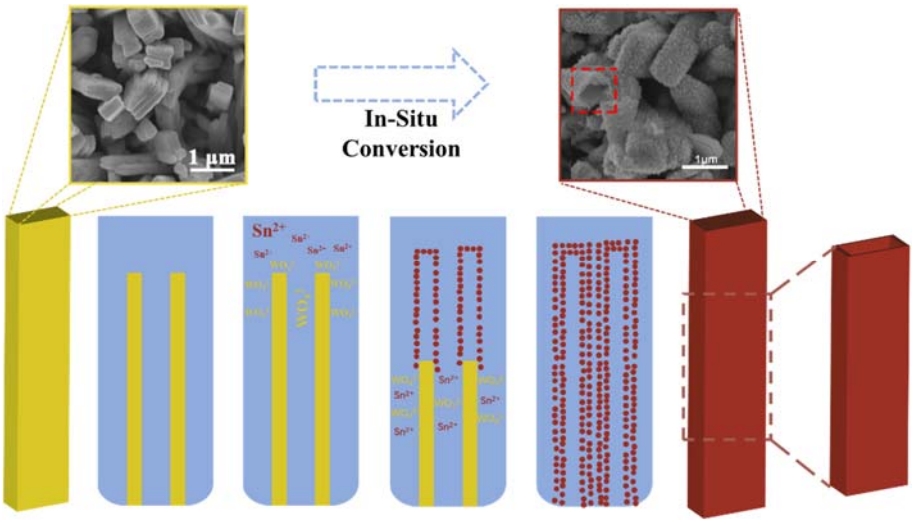

Figure 3. Schematic for in situ conversion from a rod-like WO_3 array to a rod-like $SnWO_4$ [28].

Generally speaking, $SnWO_4$ has good optical properties, such as a narrow band gap and a special band structure, which results in excellent application prospects for the fields of photocatalysis and photoelectrocatalysis (especially in the field of water splitting). However, it is necessary to pay attention to the instability and short carrier diffusion length of the material itself. Furthermore, because of the differences in crystal structure and band structure between the two crystal phases (α phase and β phase), their properties and synthesis methods are different. For instance, the photo-generated electrons (holes) of the β phase have more significant reduction (oxidation) activity than that of the α phase, so the β phase is suitable for photocatalytic degradation. The α phase has a wider light absorption range and higher carrier separation efficiency, so it has potential for use in photoelectrocatalysis.

3. Research on Modification of $SnWO_4$

Since Cho et al. first reported its optical properties in 2009 [3], $SnWO_4$ has been widely used in photocatalytic degradation [30] and photoelectrochemical water splitting [31]. Researchers have been working to modify $SnWO_4$ via morphological modification, facet regulations, doping, and the construction of multicomponent composites in order to obtain better photocatalytic degradation rates of organic pollutants (Table 1), as well as improved photoelectrochemical water splitting and sulfite oxidation performance (Table 2).

Table 1. Recently reported $SnWO_4$-based materials for photocatalysis.

Type of Catalyst	Organic Pollutant	Light	Degradation Efficiency	Ref.
Nest−like α−$SnWO_4$	methyl orange (MO)	300 W Xe arc lamp > 420 nm	96.1% (60 min)	[32]
Flower−like α−$SnWO_4$	MO	300 W tungsten-halogen lamp > 420 nm	95% (80 min)	[33]
α−$SnWO_4$ nanostrips + small nanosheets	MO	500 W Xe lamp	90.4% (30 min)	[34]
α−$SnWO_4$ synthesized with different solvents	MO	300 W Xe lamp > 420 nm	98% (80 min)	[35]
leaf−like β−$SnWO_4$	MO	250 W tungsten-halogen lamp	60% (2 h)	[36]
Bi^{3+}−doped α−$SnWO_4$	MO	500 W Xe lamp > 420 nm	95% (2 h)	[37]
α−$SnWO_4$/Ag−NPs	MO	500 W Xe lamp > 420 nm	97% (70 min)	[38]
α−$SnWO_4$/ZnFe−LDH	MO	500 W Xe lamp	95.1% (40 min)	[39]
SnS/α−$SnWO_4$	MO	500 W Xe lamp	95.6% (90 min)	[40]
CTAB−α−$SnWO_4$	MO	500 W Xe lamp	58.7% (30 min)	[20]
h−BN/α−$SnWO_4$	MO	300 W Xe lamp > 420 nm	94.7% (90 min)	[41]
α−$SnWO_4$/SnO_2	MO	500 W Xe lamp > 420 nm	97% (40 min)	[42]
β−$SnWO_4$-GO	MO	tungsten-halogen lamp > 420 nm	90% (25 min)	[12]
α−$SnWO_4$-GO	MO	300 W tungsten-halogen lamp > 420 nm	41.2% (6 h)	[43]
Zn^{2+} doped α−$SnWO_4$ nanowires	MO	300 W Hg lamp > 420 nm	~100% (90 min)	[44]
β−$SnWO_4$ with different morphology	rhodamine B (RhB)	AM 1.5 G solar light (100 mW cm^{-2})	~22% (2 h)	[45]
Cube β−$SnWO_4$	RhB	8 W UV-lamp with a monowavelength of 366 nm	TOF:1.14	[46]
Spike−cube β−$SnWO_4$	RhB	8 W UV-lamp with a monowavelength of 366 nm	TOF:2.77	[46]
SnS/α−$SnWO_4$	RhB	500 W Xe lamp	97.62% (2 h)	[40]
α−$SnWO_4$/g−C_3N_4	RhB	500 W Xe arc lamp > 420 nm	91% (80 min)	[47]
1D $ZnWO_4$@β−$SnWO_4$	RhB	300 W Xe lamp > 420 nm	~100% (2 h)	[48]
β−$SnWO_4$-GO	RhB	under visible light	91% (25 min)	[12]
α−$SnWO_4$	RhB	100 W tungsten-halogen lamp > 420 nm	~82% (4 h)	[3]
β−$SnWO_4$	RhB	100 W tungsten-halogen lamp > 420 nm	~97% (4 h)	[3]
BiOBr/α−$SnWO_4$	RhB	sunlight	97.9% (1 h)	[49]
spike−cube β−$SnWO_4$	methylene blue (MB)	8 W UV-lamp with a monowavelength of 366 nm	TOF:2.65	[43]
β−$SnWO_4$−rGO nanocomposite	MB	tungsten-halogen lamp > 420 nm	94% (2 h)	[50]
β−$SnWO_4$/ZnO	MB	70 W sodium lamps	82.9% (2 h)	[51]

β−$SnWO_4$ truncated rhombic dodecahedrons	MB	150 W halogen lamp	100% (20 min)	[19]
β−$Sn_{1-n}WO_4$·nα−Sn	MB	halogen bulb (3300 K)	~90% (1 h)	[52]
h−BN/α−$SnWO_4$	tetracycline (TC)	300 W Xe lamp > 420 nm	82.2% (4 h)	[41]
SnS/α−$SnWO_4$	TC	500 W Xe lamp	57.0% (3 h)	[40]
β−$SnWO_4$−rGO nanocomposite	rose bengal (RB)	tungsten-halogen lamp > 420 nm	98% (2 h)	[50]
β−$SnWO_4$ NPs	RB	300 W tungsten bulb	94.6% (2.5 h)	[53]
α−$SnWO_4$/UiO−66(NH_2)/g−C_3N_4	ibuprofen (IPF)	high pressure Xe lamp source simulated sunlight	95.5% (2 h)	[54]
β−$Sn_{1-n}WO_4$·nα−Sn	basic green 4 (BG)	halogen bulb (3300 K)	~63% (1 h)	[52]
BiOBr/α−$SnWO_4$	BG	sunlight	95.5% (45 min)	[49]
β−$Sn_{1-n}WO_4$·nα−Sn	methyl red (MR)	halogen bulb (3300 K)	~71% (1 h)	[52]

Table 2. Recent report on the performance of α−$SnWO_4$ based photoanodes in PEC water splitting.

Photoanode	Photocurrent Density (at 1.23 V vs. RHE)	Electrolyte	Ref.
α−$SnWO_4$ nanowires	0.032 mA cm^{-2}	0.1 M KPi buffer (pH ≈ 5)	[27]
α−$SnWO_4$ porous nanostructure	0.080 mA cm^{-2}	0.5 M KPi buffer (pH ≈ 7)	[31]
α−$SnWO_4$ nanocrystalline particles	~0.750 mA cm^{-2}	0.5 M KPi buffer and 0.5 M Na_2SO_3 (pH ≈ 7)	[4]
α−$SnWO_4$ microcrystalline particles	0.375 mA cm^{-2}	0.5 M Na_2SO_4 (pH ≈ 7)	[24]
α−$SnWO_4$ coral−like morphology	0.420 mA cm^{-2}	KOH/H_3BO_3 buffer and 0.2 M Na_2SO_3 (pH ≈ 9)	[55]
2D nanosheets α−$SnWO_4$	0.411 mA cm^{-2}	0.2 M KPi buffer (pH ≈ 7)	[56]
Nail−like α−$SnWO_4$	0.300 mA cm^{-2}	0.2 M KPi buffer (pH ≈ 7)	[29]
2D long−plate α−$SnWO_4$	0.790 mA cm^{-2}	0.2 M KPi buffer (pH ≈ 7)	[28]
NiO_x coated RTP−α−$SnWO_4$	0.950 mA cm^{-2}	0.5 M KPi buffer with 0.5 M Na_2SO_3 (pH ≈ 7)	[25]

3.1. Morphological Modification

By regulating the synthesis technique, which is a universal method for enhancing the catalytic performance of a material, a target material with a specific morphology can be obtained. The morphology of a material is usually designed for the following purposes [57]: (1) to increase the specific surface area and reduce the nanometer size, as a high specific surface area can provide more active sites, and a small nanometer size can provide a shorter charge transfer path that improves carrier separation efficiency and enhances light absorption efficiency; (2) to improve the crystallinity of materials, as a high crystallinity

can reduce the recombination center and improve carrier separation efficiency, but it is difficult to simultaneously improve crystallinity and specific surface area; (3) to obtain special structural shapes (such as 0D, 1D, 2D, and 3D materials), as different dimensions have diverse characteristics. Thus, directional design can improve the performance of the materials.

In the study of $SnWO_4$ for photocatalysis, there have been many attempts to obtain improved properties by adjusting the morphologies of the substrate materials. Zhu et al. obtained flower−like α−$SnWO_4$ powders under neutral conditions with a DTAB−assisted hydrothermal method, degrading 95% of methyl orange (MO) within 80 min [33]. Want et al. also discussed the solvent-dependent morphology of α−$SnWO_4$ powders [35], and Liu et al. synthesized nanostrips and nanosheets by changing the water/ethylene glycol ratio through a solvothermal method [34]. Meanwhile, the layered multi-hollow spherical α−$SnWO_4$ powders [37] prepared by Zhu et al. and the nested nanostructure α−$SnWO_4$ [32] prepared by Zhang et al. showed an improved catalytic performance after controlling their morphologies. The increased specific surface area enabled by morphology controlling exposes the active sites and shortens the length needed for photo-generated carriers to arrive at a surface. For a β−$SnWO_4$ photocatalyst, Chen et al. prepared cubes and spike−cube shaped particles, with the latter showing strong photocatalytic activity [46]. Warmuth et al. formed tetrahedral β−$SnWO_4$, which demonstrated better photodegradation activity than a β−$SnWO_4$ material, with truncated octahedra and a spike−cube morphology (Figure 4a) [45]. Ungelenk et al. synthesized β−$SnWO_4$ powders with a microemulsion method. The powders had a rhombohedral dodecahedron shape, and they could complete the degradation of methylene blue (MB) in 20 min [19]. Raj et al. also noted the better MO degradation performance of leaf−like β−$SnWO_4$ compared with that of sphere−like and irregularly structured β−$SnWO_4$ [36]. Alharthi et al. synthesized honeycomb−like β−$SnWO_4$ with a hydrothermal method and calcined it at 700 °C, which enabled the photodegradation of rose bengal in 150 min [53]. For photoelectrochemical water splitting, it is difficult to control the morphology of the powder present on an electrode. Accordingly, Zhu et al. synthesized a porous α−$SnWO_4$ film through the hydrothermal conversion of WO_3 films [31], and they obtained a photocurrent density of 0.08 $mA \cdot cm^{-2}$ at a potential of 1.23 V_{RHE}. In contrast, topography optimized nails (Figure 4b) [27, 29], nanosheets (Figure 4c) [56], and long−plates [28] have presented better PEC activity than α−$SnWO_4$, with a powder stacked morphology because the array structures provide pathways for charge transfer, with less recombination.

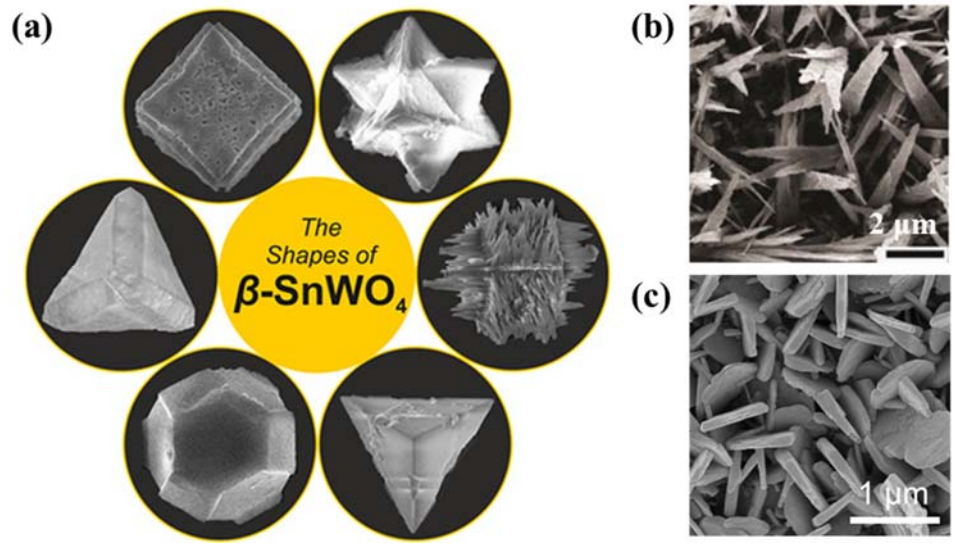

Figure 4. (**a**) Different shapes of β−$SnWO_4$ [45]; α−$SnWO_4$ with (**b**) dense nanorods [27] and (**c**) nanosheet [56] morphology.

3.2. Crystal Facet Engineering

During morphology regulation, the ratio of exposure facets may change as well [58]. It is noted that reaction activities vary for different facets [59, 60]. Thus, charge transfer ability can be modified by controlling the anisotropic growth of crystals in a certain direction. The β–$SnWO_4$ enclosed by (100) and (110) facets obtained the strong photocatalytic degradation of methylene blue [19]. Harb et al. found that the (001) facet of α–$SnWO_4$ and the (100) facet of β–$SnWO_4$ showed strong charge separation and transport capabilities via calculations with the HSE06 code [10]. They also discussed the (121), (210), (111), (200), and (040) exposed facets of α–$SnWO_4$ using DFT, and the (210) and (121) facets were shown to perform oxygen evolution reaction due to the positive position of their valence band (Figure 5a) [61]. They also noted that the (001) facet had a high surface energy, but it may be thermodynamically less stable than the other five facets. Wang et al. discussed the oxygen evolution performance of α–$SnWO_4$ (010) facets with different kinds of termination, and O–Sn termination showed better OER activity than did the others [62]. These DFT researchers have demonstrated that crystal facet engineering is another viable method for obtaining a good $SnWO_4$ substrate material. Inspired by these projects, our group synthesized an α–$SnWO_4$ array and added F ions to its precursor solution to increase the ratio of the (001) facet (Figure 5b). The facet-controlled film had a higher photocurrent than the uncontrolled film due to the better OER performance (Figure 5c) [29], and a ~1.9 times greater photocurrent was obtained in an unbiased PEC cell.

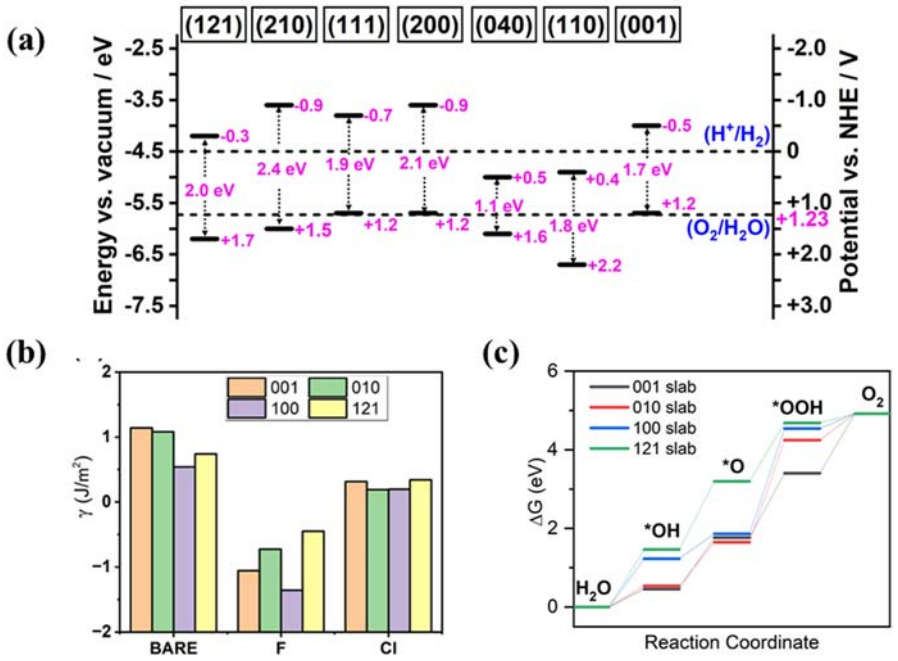

Figure 5. (**a**) VBM and CBM energy levels for the optimized (121)–, (210)–, (111)–, (200)–, (040)–, (110), and (001) oriented α–$SnWO_4$ slabs [61, 63]; (**b**) surface free energy (γ) of facets before and after the termination with F and Cl atoms; (**c**) free–energy profiles of OER on (001)–, (010)–, (100)–, and (121) slabs at 0 V (the * means adsorbed state) [29].

3.3. Doping Modification

Doping can change the position of an energy band, reduce the width of a band gap, and improve the efficiency of carrier separation and transfer, thus improving the catalytic performance of the materials. For example, Zn^{2+} doping was introduced into α–$SnWO_4$ by Su et al. [44]. Because Zn and Sn have similar electronegativity values and suitable sizes, Zn^{2+} is used to replace Sn^{2+} in $SnWO_4$ to form $Sn_{1-x}Zn_xWO_4$. This ensures that the Zn 4s and Zn 4p orbitals participate in the hybridization of the valence band and the conduction band, respectively, thus changing the position of the energy band and reducing the band

gap. The authors also found that Zn^{2+} doping changed the morphology of the material, and the resulting $Sn_{0.955}Zn_{0.045}WO_4$ could degrade nearly 90% of MO in 20 min. Zhu et al. introduced defects into α−$SnWO_4$ through Bi^{3+} doping [37]. Unlike Zn^{2+} doping, Bi does not participate in the formation of energy band hybridization, but cation vacancies are formed due to changes in the charges. These defects form effective energy levels in the band gap which enhance light absorption, inhibit electron−hole pairing, and improve the photocatalytic properties of the material. Although the mechanisms of Zn^2 and Bi^3 doping are not exactly the same, both of them can improve the performance of $SnWO_4$ by changing its morphology and band structure. At the same time, because β−$SnWO_4$ has a wider band and a lower carrier separation efficiency than α−$SnWO_4$, the doping of the two ions may lead to better performance improvements for β−$SnWO_4$. In addition to these two kinds of hetero ions, there may be more suitable ions for $SnWO_4$ modification (such as Mo and Co) that need to be further studied. In theory, Azofra et al. replaced Sn with Ge and substituted W with Mo in DFT calculations, and they obtained the enhanced orbital hybridization of the VBM/CBM electronic states, which amplified the amount of generated holes/electrons on top of the (110)/(100) facets [63]. However, these result have not been experimentally confirmed.

3.4. Multicomponent Composite

The multicomponent composite strategy includes coating a sedimentary protection layer and building heterojunction. Constructed multicomponent catalysts generally have the following advantages over single catalysts: (1) they expand the light absorption spectra, (2) they promote carrier separation, (3) they inhibit carrier recombination, and (4) they prevent photocorrosion.

In photocatalysis, the compositing of reduced graphene oxide (RGO) and β−$SnWO_4$ can be achieved via microwave heating [12] and hydrothermal methods [50]. In such a composite, RGO, as a supporting material, provides a larger surface area and more active sites than β−$SnWO_4$, thereby improving the specific surface area and catalytic activity of the material. At the same time, the high conductivity of RGO makes the electrons generated by β−$SnWO_4$ move towards the RGO, while the holes remain inside β−$SnWO_4$, which improves the carrier separation efficiency of the materials. The compositing of RGO and α−$SnWO_4$ was reported by Huang et al. [43], and Wang et al.[41] combined hexagonal boron nitride (2D materials analogous to graphite) with α−$SnWO_4$. Both groups improved the photocatalytic activity of α−$SnWO_4$ for degrading methyl orange (MO) and tetracycline. In a composite of Ag-NPs and α−$SnWO_4$ [38], the photo-absorption efficiency can be increased through the surface plasmon resonance (SPR) of Ag-NPs. Because Ag-NPs have lower Fermi levels than the bottom of the conduction band of α−$SnWO_4$, the photoelectrons can migrate to Ag, increasing the efficiency of carrier separation. Moreover, Ag can more easily transfer electrons to a solution when it is in direct contact with the solution, which accelerates the transfer of interfacial carriers. The construction of heterojunctions is widely studied in $SnWO_4$ material research. The formation of heterojunctions is mainly based on the combination of different energy band positions of different materials. Accordingly, photogenerated electrons are easier to transfer to materials with lower conduction bands, while photogenerated holes tend to transfer to materials with higher valence bands. It is possible to enhance the carrier separation efficiency of materials by selecting suitable materials for compositing. For example, the heterojunctions of α−$SnWO_4$ and g−C_3N_4 were shown to effectively inhibit carrier recombination, thereby increasing the catalytic activity of the material [47]. $SnWO_4$/ZnO [51], $SnWO_4$/BiOBr [49], $SnWO_4$/UiO−66/g−C_3N_4 ternary heterojunction [54], one dimensional $ZnWO_4$@$SnWO_4$ core−shell heterojunction [48], and SnS/α−$SnWO_4$ [40] have also been reported. In addition, α−$SnWO_4$ and SnO_2 [42], along with β−$SnWO_4$ [52], can form heterojunctions to improve the efficiency of carrier separation.

In photoelectrocatalysis, Kölbach and Schnell et al. deposited NiO_x on α−$SnWO_4$ to protect the substrate from photocorrosion [4], which improved material stability and

maintained a stable current for sulfite oxidation at 1.23 V vs. RHE in 30 min. Furthermore, α−$SnWO_4$ is susceptible to photo−corrosion and oxidation during photoelectrochemical water splitting, which results in a lower photocurrent value (<10 $\mu A \cdot cm^{-2}$). However, the photocurrent of the material is greatly increased after protection by NiO_x (~0.75 $mA \cdot cm^{-2}$). Another study found that a thin oxide layer (SnO_2) might form at the interface of α−$SnWO_4$ and NiO_x, which explains the reason for the decreasing photovoltage after the loading of NiO_x [9]. Thus, the exploration of alternative techniques for loading protection layers, such as vacuum evaporation and atomic layer deposition, is recommended.

3.5. Other Techniques

In addition to the aforementioned approaches, photocatalysis and photoelectrocatalysis performance may be influenced by the external environment [64], as has been studied in recent years. Liu et al. discussed the PEC performance of $SnWO_4$/Sn electrodes at different operating temperatures, and they found that higher photocurrents could be obtained at 70 °C (Figure 6a) [55]. Schnell studied the pH−dependent stability of α−$SnWO_4$, and pH = 7 (Figure 6b) was suggested to be used for testing due to the formation of the surface oxide layer as a protection layer [65]. Besides, α−$SnWO_4$, with higher crystallinity, was formed by Cottesman, presenting ~0.95 mA/cm^2 after loading with NiO_x for sulfite oxidation.

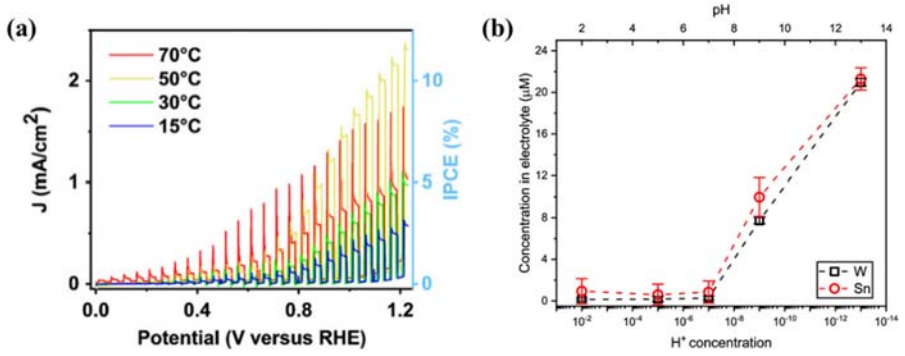

Figure 6. (**a**) LSV curves of the $SnWO_4$ (500 °C H_2) photoanode measured in KOH/H_3BO_3 buffer (pH = 9) with 0.2 M Na_2SO_3 at different temperatures under the chopped 455 nm LED illumination [55]; (**b**) the concentrations of Sn and W dissolved from α−$SnWO_4$ films after photoelectrochemically treated at various pH levels at a potential of 1.23 V vs. RHE, for a total of 1 h [65].

4. Conclusions and Outlook

In general, $SnWO_4$ is considered a type of potential catalytic material for photocatalysis and photoelectrocatalysis, especially for water splitting, because of its optical properties and special band structure (which covers the oxidation and reduction potential of water). β−$SnWO_4$ is always used in photocatalytic degradation due to the high reduction (oxidation) activity of its photo-generated electrons (holes), while α−$SnWO_4$ is employed in both photocatalysis and photoelectrocatalysis. In recent years, many researchers have studied the application of $SnWO_4$ in photocatalysis and photoelectrocatalysis, and they have improved the properties of materials by means of morphology control, doping, and multicomponent combinations. Compared with photocatalysis, photoelectrocatalysis has the advantage of discrete oxidation and reduction processes. This makes it easier to separate gaseous products, study reaction mechanisms and kinetics, and adjust reaction selectivity. Therefore, the application of α−$SnWO_4$ in photoelectrocatalysis needs to be further explored. However, it is worth noting that the catalytic performance of α−$SnWO_4$ and its applications in solar energy have not reached their expected values. For example, the highest reported experimental current for PEC water oxidation is only ~0.79 $mA \cdot cm^{-2}$ at 1.23 V_{RHE}, which is far from the theoretical value. Other problems include low efficiency and poor stability. To solve these problems, obtaining a high-performing substrate

through morphology control, crystal surface control, and doping may prove to be an effective research route. Then, the PEC performance of α–$SnWO_4$ can be further upgraded by constructing heterojunctions, depositing protective layers, and depositing cocatalysts. Of these methods, loading cocatalysts is the most promising because the catalysts can also act as protection layers. However, a suitable loading method to avoid oxidizing α–$SnWO_4$ is required, and pinholes should be excluded to prevent α–$SnWO_4$ from attaching to the electrolytes.

Author Contributions: W.Q.: writing—original draft and visualization; Y.L.: writing—review and editing, supervision, funding acquisition, and conceptualization. All authors have read and agreed to the published version of the manuscript.

Funding: This study was supported by the National Nature Science Foundation of China (51904356).

Data Availability Statement: Not applicable.

Acknowledgments: W.Q. and Y.L. appreciate GaoShuang He, Keke Wang, Wenzhang Li, and Jie Li's suggestions on this paper.

Conflicts of Interest: The authors declare no conflict of interest.

References

1. Fujishima, A.; Honda, K. Electrochemical Photolysis of Water at a Semiconductor Electrode. *Nature* **1972**, *238*, 37–38.
2. Tao, X.; Zhao, Y.; Wang, S.; Li, C.; Li, R. Recent advances and perspectives for solar-driven water splitting using particulate photocatalysts. *Chem. Soc. Rev.* **2022**, *51*, 3561–3608. https://doi.org/10.1039/D1CS01182K.
3. Cho, I.-S.; Kwak, C.H.; Kim, D.W.; Lee, S.; Hong, K.S. Photophysical, Photoelectrochemical, and Photocatalytic Properties of Novel $SnWO_4$ Oxide Semiconductors with Narrow Band Gaps. *J. Phys. Chem. C* **2009**, *113*, 10647–10653. https://doi.org/10.1021/jp901557z.
4. Kölbach, M.; Pereira, I.J.; Harbauer, K.; Plate, P.; Höflich, K.; Berglund, S.P.; Friedrich, D.; van de Krol, R.; Abdi, F.F. Revealing the performance limiting factors in α-$SnWO_4$ photoanodes for solar water splitting. *Chem. Mater.* **2018**, *30*, 8322–8331. https://doi.org/10.1021/acs.chemmater.8b03883.
5. Jeitschko, W.; Sleight, A. Stannous tungstate: Properties, crystal structure and relationship to ferroelectric $SbTaO_4$ type compounds. *Acta Crystallogr. Sect. B Struct. Crystallogr. Cryst. Chem.* **1974**, *30*, 2088–2094.
6. Jeitschko, W.; Sleight, A.W. Synthesis, properties and crystal structure of β-$SnWO_4$. *Acta Crystallogr. Sect. B Struct. Crystallogr. Cryst. Chem.* **1972**, *28*, 3174–3178, doi:doi:10.1107/S056774087200768X.
7. Ke, J.; Younis, M.A.; Kong, Y.; Zhou, H.; Liu, J.; Lei, L.; Hou, Y. Nanostructured Ternary Metal Tungstate-Based Photocatalysts for Environmental Purification and Solar Water Splitting: A Review. *Nano-Micro Lett.* **2018**, *10*, 69. https://doi.org/10.1007/s40820-018-0222-4.
8. Gomes, E.O.; Gouveia, A.F.; Gracia, L.; Lobato, A.; Recio, J.M.; Andres, J. A Chemical-Pressure-Induced Phase Transition Controlled by Lone Electron Pair Activity. *J. Phys. Chem. Lett.* **2022**, *13*, 9883–9888. https://doi.org/10.1021/acs.jpclett.2c02582.
9. Schnell, P.; Kolbach, M.; Schleuning, M.; Obata, K.; Irani, R.; Ahmet, I.Y.; Harb, M.; Starr, D.E.; van de Krol, R.; Abdi, F.F. Interfacial Oxide Formation Limits the Photovoltage of α-$SnWO_4$/NiO_x Photoanodes Prepared by Pulsed Laser Deposition. *Adv. Energy Mater.* **2021**, *11*, 2003183. https://doi.org/10.1002/aenm.202003183.
10. Harb, M.; Ziani, A.; Takanabe, K. Critical difference between optoelectronic properties of α- and β-$SnWO_4$ semiconductors: A DFT/HSE06 and experimental investigation. *Phys. Status Solidi B* **2016**, *253*, 1115–1119, doi:doi:10.1002/pssb.201552774.
11. Kuzmin, A.; Anspoks, A.; Kalinko, A.; Timoshenko, J.; Kalendarev, R. Extended x-ray absorption fine structure spectroscopy and first-principles study of $SnWO_4$. *Phys. Scr.* **2014**, *89*, 044005.
12. Thangavel, S.; Venugopal, G.; Kim, S.-J. Enhanced photocatalytic efficacy of organic dyes using β-tin tungstate–reduced graphene oxide nanocomposites. *Mater. Chem. Phys.* **2014**, *145*, 108–115. https://doi.org/10.1016/j.matchemphys.2014.01.046.
13. Alexei, K.; Andris, A.; Aleksandr, K.; Janis, T.; Robert, K.; Lucie, N.; François, B.; Tetsuo, I.; Pascale, R. Pressure-induced insulator-to-metal transition in α-$SnWO_4$. *J. Phys. Conf. Ser.* **2016**, *712*, 012122.

14. Kuzmin, A.; Zubkins, M.; Kalendarev, R. Preparation and Characterization of Tin Tungstate Thin Films. *Ferroelectrics* **2015**, *484*, 49–54. https://doi.org/10.1080/00150193.2015.1059682.
15. Ziani, A.; Harb, M.; Noureldine, D.; Takanabe, K. UV-Vis optoelectronic properties of α-$SnWO_4$: A comparative experimental and density functional theory based study. *APL Mater.* **2015**, *3*, 096101. https://doi.org/10.1063/1.4930005.
16. Stoltzfus, M.W.; Woodward, P.M.; Seshadri, R.; Klepeis, J.-H.; Bursten, B. Structure and Bonding in $SnWO_4$, $PbWO_4$, and $BiVO_4$: Lone Pairs vs. Inert Pairs. *Inorg. Chem.* **2007**, *46*, 3839–3850. https://doi.org/10.1021/ic061157g.
17. Wojcik, J.; Calvayrac, F.; Goutenoire, F.; Mhadhbi, N.; Corbel, G.; Lacorre, P.; Bulou, A. Lattice Dynamics of β-$SnWO_4$: Experimental and Ab Initio Calculations. *J. Phys. Chem. C* **2013**, *117*, 5301–5313. https://doi.org/10.1021/jp3099126.
18. Pavithra, N.S.; Patil, S.B.; Kumar, S.R.K.; Alharthi, F.A.; Nagaraju, G. Facile synthesis of nanocrystalline β-$SnWO_4$: As a photocatalyst, biosensor and anode for Li-ion battery. *SN Appl. Sci.* **2019**, *1*, 1123. https://doi.org/10.1007/s42452-019-1163-3.
19. Ungelenk, J.; Feldmann, C. Synthesis of faceted β-$SnWO_4$ microcrystals with enhanced visible-light photocatalytic properties. *Chem. Commun.* **2012**, *48*, 7838–7840. https://doi.org/10.1039/c2cc33224h.
20. Huang, J.; Liu, H.; Zhong, J.; Li, J. Enhanced simulated sunlight-driven photocatalytic performance of $SnWO_4$ prepared in the presence of cetyltrimethylammonium bromide. *Environ. Prog. Sustain. Energy* **2020**, *39*, e13314. https://doi.org/10.1002/ep.13314.
21. Alharthi, F.A.; Shashank, M.; Shashikanth, J.; Viswantha, R.; Alghamdi, A.A.; Algethami, J.; Alsaiari, M.A.; Jalalah, M.S.; Ganganagappa, N. Hydrothermal synthesis of α-$SnWO_4$: Application to lithium-ion battery and photocatalytic activity. *Ceram. Int.* **2021**, *47*, 10242–10249. https://doi.org/10.1016/j.ceramint.2020.10.122.
22. Barros, M.M.P.; Almeida, K.C.; Silva, S.A.; Botelho, G. Synthesis and characterization of α-$SnWO_4$ powders obtained by microwave-assisted hydrothermal method. *Cerâmica* **2022**, *68*, 236–241. https://doi.org/10.1590/0366-69132022683863259.
23. Kölbach, M.; Hempel, H.; Harbauer, K.; Schleuning, M.; Petsiuk, A.; Höflich, K.; Deinhart, V.; Friedrich, D.; Eichberger, R.; Abdi, F.F.; et al. Grain Boundaries Limit the Charge Carrier Transport in Pulsed Laser Deposited α-$SnWO_4$ Thin Film Photoabsorbers. *ACS Appl. Energy Mater.* **2020**, *3*, 4320–4330. https://doi.org/10.1021/acsaem.0c00028.
24. Bozheyev, F.; Akinoglu, E.M.; Wu, L.; Lu, H.; Nemkayeva, R.; Xue, Y.; Jin, M.; Giersig, M. Band gap optimization of tin tungstate thin films for solar water oxidation. *Int. J. Hydrogen Energy* **2020**, *45*, 8676–8685. https://doi.org/10.1016/j.ijhydene.2020.01.126.
25. Gottesman, R.; Peracchi, I.; Gerke, J.L.; Irani, R.; Abdi, F.F.; van de Krol, R. Shining a Hot Light on Emerging Photoabsorber Materials: The Power of Rapid Radiative Heating in Developing Oxide Thin-Film Photoelectrodes. *Acs Energy Lett.* **2022**, *7*, 514–522. https://doi.org/10.1021/acsenergylett.1c02220.
26. Zhu, S.; Liu, D.; Li, J.; Kuang, Y. Chemical Vapor Deposition of Crystalized Nanoscale α-SnWO4 Thin Films and Their Photoelectrocatalytic Properties. *ACS Appl. Energy Mater.* **2022**, *5*, 14372–14380. https://doi.org/10.1021/acsaem.2c02909.
27. Pyper, K.J.; Evans, T.C.; Bartlett, B.M. Synthesis of α-$SnWO_4$ thin-film electrodes by hydrothermal conversion from crystalline WO_3. *Chin. Chem. Lett.* **2015**, *26*, 474–478. https://doi.org/10.1016/j.cclet.2015.01.027.
28. Qiu, W.; Zhang, Y.; He, G.; Chen, L.; Wang, K.; Wang, Q.; Li, W.; Liu, Y.; Li, J. Two-Dimensional Long-Plate $SnWO_4$ Photoanode Exposed Active Facets for Enhanced Solar Water Splitting. *ACS Appl. Energy Mater.* **2022**, *5*, 11732–11739. https://doi.org/10.1021/acsaem.2c02235.
29. Liu, Y.; Qiu, W.; He, G.; Wang, K.; Wang, Y.; Chen, L.; Wu, Q.; Li, W.; Li, J. Nail-like α-$SnWO_4$ Array Film with Increased Reactive Facets for Photoelectrochemical Water Splitting. *J. Phys. Chem. C* **2022**, *126*, 15596–15605. https://doi.org/10.1021/acs.jpcc.2c04302.
30. Mirsadeghi, S.; Zandavar, H.; Tooski, H.F.; Rahimi, M.; Sohouli, E.; Rahimi-Nasrabadi, M.; Ganjali, M.R.; Pourmortazavi, S.M. Rapid photodegradation and detection of zolpidem over β-$SnWO_4$ and α-$SnWO_4$ nanoparticles: Optimization and mechanism. *Environ. Sci. Pollut. Res.* **2020**, *28*, 5430–5442. https://doi.org/10.1007/s11356-020-10820-1.
31. Zhu, Z.; Sarker, P.; Zhao, C.; Zhou, L.; Grimm, R.L.; Huda, M.N.; Rao, P.M. Photoelectrochemical Properties and Behavior of α-$SnWO_4$ Photoanodes Synthesized by Hydrothermal Conversion of WO_3 Films. *ACS Appl. Mater. Interfaces* **2017**, *9*, 1459–1470. https://doi.org/10.1021/acsami.6b12640.

32. Zhang, X.; You, X.; Wang, X.; Yu, C.; Xu, L.; Wang, C.; Song, Y.; Zhang, F. Nest-like α-$SnWO_4$ nanostructures assembled by nanowires: Facile synthesis and their superior photocatalytic performance. *J. Alloy. Compd.* **2019**, *802*, 502–510. https://doi.org/10.1016/j.jallcom.2019.06.248.
33. Zhu, G.; Que, W.; Zhang, J.; Zhong, P. Photocatalytic activity of $SnWO_4$ and SnW_3O_9 nanostructures prepared by a surfactant-assisted hydrothermal process. *Mater. Sci. Eng., B* **2011**, *176*, 1448–1455. https://doi.org/10.1016/j.mseb.2011.08.003.
34. Liu, X.; Liang, B.; Yang, J.; Li, W. Solvent effect on morphological evolution and photocatalytic property of α-$SnWO_4$. *J. Taiwan Inst. Chem. Eng.* **2019**, *95*, 575–582. https://doi.org/10.1016/j.jtice.2018.09.014.
35. Wang, Q.L.; Li, H.B.; Jiang, H.Y.; Ding, S.T.; Song, Z.W.; Shi, J.S. Effect of solvent on α-$SnWO_4$ photocatalyst for degradation of methyl orange under visible light irradiation. *Adv. Perform. Mater.* **2015**, *30*, 288–293. https://doi.org/10.1179/1753555714y.0000000262.
36. Raj, A.T.; Thangavel, S.; Rose, A.; Jipsa, C.V.; Jose, M.; Nallamuthu, G.; Kim, S.-J.; Venugopal, G. Influence of Morphology and Common Oxidants on the Photocatalytic Property of β-$SnWO_4$ Nanoparticles. *J. Nanosci. Nanotechnol.* **2016**, *16*, 2541–2547. https://doi.org/10.1166/jnn.2016.10961.
37. Zhu, Z.; Tian, H.; Zhang, M.; Liang, B.; Li, W. Preparation of α-$SnWO_4$ hierarchical spheres by Bi^{3+}-doping and their enhanced photocatalytic activity under visible light. *Ceram. Int.* **2016**, *42*, 14743–14748. https://doi.org/10.1016/j.ceramint.2016.06.101.
38. Liu, X.; Liang, B.; Zhang, M.; Long, Y.; Li, W. Enhanced photocatalytic properties of α-$SnWO_4$ nanosheets modified by Ag nanoparticles. *J. Colloid Interface Sci.* **2017**, *490*, 46–52. https://doi.org/10.1016/j.jcis.2016.11.029.
39. Wang, Y.; Zhou, S.; Zhao, G.; Li, C.; Liu, L.; Jiao, F. Fabrication of SnWO4/ZnFe-layered double hydroxide composites with enhanced photocatalytic degradation of methyl orange. *J. Mater. Sci.-Mater. Electron.* **2020**, *31*, 12269–12281. https://doi.org/10.1007/s10854-020-03772-2.
40. Liu, X.; Liang, B.; Li, W. In situ decoration of SnS quantum dots on the α-$SnWO_4$ nanosheets for superior visible-light photocatalytic performance. *Appl. Surf. Sci.* **2020**, *531*, 147379. https://doi.org/10.1016/j.apsusc.2020.147379.
41. Wang, J.; Yan, H.; Long, Y.; Li, W. Enhanced photocatalytic property of α-$SnWO_4$ nanoplates by h-BN decorating. *J. Mater. Sci. Mater. Electron.* **2021**, *32*, 21858–21868. https://doi.org/10.1007/s10854-021-06530-0.
42. Yao, S.; Zhang, M.; Di, J.; Wang, Z.; Long, Y.; Li, W. Preparation of α-$SnWO_4$/SnO_2 heterostructure with enhanced visible-light-driven photocatalytic activity. *Appl. Surf. Sci.* **2015**, *357*, 1528–1535. https://doi.org/10.1016/j.apsusc.2015.10.012.
43. Huang, R.K.; Ge, H.; Lin, X.J.; Guo, Y.L.; Yuan, R.S.; Fu, X.Z.; Li, Z.H. Facile one-pot preparation of α-$SnWO_4$/reduced graphene oxide (RGO) nanocomposite with improved visible light photocatalytic activity and anode performance for Li-ion batteries. *Rsc Adv.* **2013**, *3*, 1235–1242. https://doi.org/10.1039/c2ra22054g.
44. Su, Y.G.; Hou, L.C.; Du, C.F.; Peng, L.M.; Guan, K.; Wang, X.J. Rapid synthesis of Zn^{2+} doped $SnWO_4$ nanowires with the aim of exploring doping effects on highly enhanced visible photocatalytic activities. *Rsc Adv.* **2012**, *2*, 6266–6273. https://doi.org/10.1039/c2ra20401k.
45. Warmuth, L.; Feldmann, C. β-$SnWO_4$ with Morphology-Controlled Synthesis and Facet-Depending Photocatalysis. *ACS Omega* **2019**, *4*, 13400–13407. https://doi.org/10.1021/acsomega.9b01593.
46. Chen, Y.-C.; Lin, Y.-G.; Hsu, L.-C.; Tarasov, A.; Chen, P.-T.; Hayashi, M.; Ungelenk, J.; Hsu, Y.-K.; Feldmann, C. β-$SnWO_4$ Photocatalyst with Controlled Morphological Transition of Cubes to Spikecubes. *ACS Catal.* **2016**, *6*, 2357–2367. https://doi.org/10.1021/acscatal.5b02444.
47. Liang, Q.; Jin, J.; Liu, C.; Xu, S.; Yao, C.; Chen, Z.; Li, Z. Hydrothermal fabrication of α-$SnWO_4$/g-C_3N_4 heterostructure with enhanced visible-light photocatalytic activity. *J. Mater. Sci.: Mater. Electron.* **2017**, *28*, 11279–11283. https://doi.org/10.1007/s10854-017-6918-2.
48. Zhuang, H.; Xu, W.; Lin, L.; Huang, M.; Xu, M.; Chen, S.; Cai, Z. Construction of one dimensional $ZnWO_4$@$SnWO_4$ core-shell heterostructure for boosted photocatalytic performance. *J. Mater. Sci. Technol.* **2019**, *35*, 2312–2318. https://doi.org/10.1016/j.jmst.2019.05.036.
49. Chowdhury, A.P.; Shambharkar, B.H. Fabrication and characterization of BiOBr-SnWO4 heterojunction nanocomposites with boosted photodegradation capability. *Chem. Eng. J. Adv.* **2020**, *4*, 100040. https://doi.org/10.1016/j.ceja.2020.100040.
50. Alharthi, F.A.; Alsaiari, M.A.; Jalalah, M.S.; Shashank, M.; Shashikanth; Alghamdi, A.A.; Algethami, J.S.; Ganganagappa, N. Combustion synthesis of β-$SnWO_4$-rGO: Anode material for Li-ion battery and photocatalytic dye degradation. *Ceram. Int.* **2021**, *47*, 10291–10300. https://doi.org/10.1016/j.ceramint.2020.07.142.

51. Elviera; Yulizar, Y.; Apriandanu, D.O.B.; Surya, R.M. Fabrication of novel $SnWO_4$/ZnO using Muntingia calabura L. leaf extract with enhanced photocatalytic methylene blue degradation under visible light irradiation. *Ceram. Int.* **2022**, *48*, 3564–3577. https://doi.org/10.1016/j.ceramint.2021.10.135.
52. Ungelenk, J.; Feldmann, C. Nanoscale β-$Sn_{1-n}WO_4$·nα-Sn-A highly efficient photocatalyst for daylight-driven degradation of organic dyes and its real "green" synthesis. *Appl. Catal. B-Environ.* **2011**, *102*, 515–520. https://doi.org/10.1016/j.apcatb.2010.12.033.
53. Alharthi, F.A.; AlFawaz, A.; Ahmad, N. Photocatalytic degradation of anionic dye using well-crystalline $SnWO_4$ polyoxometalate. *Phys. Scr.* **2022**, *97*, 085813. https://doi.org/10.1088/1402-4896/ac7d7a.
54. Wei, Q.; Xiong, S.; Li, W.; Jin, C.; Chen, Y.; Hou, L.; Wu, Z.; Pan, Z.; He, Q.; Wang, Y.; et al. Double Z-scheme system of α-$SnWO_4$/UiO-66(NH_2)/g-C_3N_4 ternary heterojunction with enhanced photocatalytic performance for ibuprofen degradation and H_2 evolution. *J. Alloy. Compd.* **2021**, *885*, 160984. https://doi.org/10.1016/j.jallcom.2021.160984.
55. Liu, D.; Chen, X.; Qiao, Y.; Zhou, Y.; Kuang, Y. Awakening the Photoelectrochemical Activity of α-$SnWO_4$ Photoanodes with extraordinary Crystallinity Induced by Reductive Annealing. *Adv. Energy Sustain. Res.* **2021**, *3*, 2100146. https://doi.org/10.1002/aesr.202100146.
56. He, G.; Li, W.; Qiu, W.; Xu, C.; Wang, K.; Chen, L.; Wang, Y.; Liu, Y.; Li, J. Constructing a Two-Dimensional $SnWO_4$ Nanosheet Array Film for Enhanced Photoelectrochemical Performance. *ACS Appl. Energy Mater.* **2022**, *5*, 11883–11891. https://doi.org/10.1021/acsaem.2c02547.
57. Wu, H.; Tan, H.L.; Toe, C.Y.; Scott, J.; Wang, L.; Amal, R.; Ng, Y.H. Photocatalytic and Photoelectrochemical Systems: Similarities and Differences. *Adv Mater* **2019**, *32*, 1904717. https://doi.org/10.1002/adma.201904717.
58. Liu, Y.; Wygant, B.R.; Kawashima, K.; Mabayoje, O.; Hong, T.E.; Lee, S.-G.; Lin, J.; Kim, J.-H.; Yubuta, K.; Li, W.; et al. Facet effect on the photoelectrochemical performance of a WO_3/$BiVO_4$ heterojunction photoanode. *Appl. Catal. B* **2019**, *245*, 227–239. https://doi.org/10.1016/j.apcatb.2018.12.058.
59. Chen, L.; Li, W.; Qiu, W.; He, G.; Wang, K.; Liu, Y.; Wu, Q.; Li, J. Oriented $CuWO_4$ Films for Improved Photoelectrochemical Water Splitting. *ACS Appl. Energy Mater.* **2022**, *14*, 47737–47746. https://doi.org/10.1021/acsami.2c13002.
60. Liu, C.; Chen, L.; Su, X.; Chen, S.; Zhang, J.; Yang, H.; Pei, Y. Activating a TiO_2/$BiVO_4$ Film for Photoelectrochemical Water Splitting by Constructing a Heterojunction Interface with a Uniform Crystal Plane Orientation. *ACS Appl. Energy Mater.* **2022**, *14*, 2316–2325. https://doi.org/10.1021/acsami.1c20038.
61. Harb, M.; Cavallo, L.; Basset, J.-M. Remarkable Influence of α-$SnWO_4$ Exposed Facets on Their Photocatalytic Performance for H_2 and O_2 Evolution Reactions. *J. Phys. Chem. C* **2020**, *124*, 18684–18689. https://doi.org/10.1021/acs.jpcc.0c06718.
62. Wang, W.; Wu, Y.; Chen, D.-L.; Liu, H.; Xu, M.; Liu, X.; Xin, L. The surface reconstruction induced enhancement of the oxygen evolution reaction on α-$SnWO_4$ (010) based on a density functional theory study. *Phys. Chem. Chem. Phys.* **2022**, *24*, 19382–19392. https://doi.org/10.1039/d2cp02159e.
63. Azofra, L.M.; Cavallo, L.; Basset, J.-M.; Harb, M. Need for Rationally Designed $SnWO_4$ Photo(electro)catalysts to Overcome the Performance Limitations for O_2 and H_2 Evolution Reactions. *J. Phys. Chem. C* **2021**, *125*, 8488–8496. https://doi.org/10.1021/acs.jpcc.0c11614.
64. Liu, Y.; Chen, L.; Zhu, X.; Qiu, H.; Wang, K.; Li, W.; Cao, S.; Zhang, T.; Cai, Y.; Wu, Q.; et al. Effects of operating temperature on photoelectrochemical performance of $CuWO_4$ film photoanode. *J. Electroanal. Chem.* **2022**, *924*, 116859. https://doi.org/10.1016/j.jelechem.2022.116859.
65. Schnell, P.; Dela Cruz, J.M.C.M.; Kölbach, M.; van de Krol, R.; Abdi, F.F. pH-Dependent Stability of α-$SnWO_4$ Photoelectrodes. *Chem. Mater.* **2022**, *34*, 1590–1598. https://doi.org/10.1021/acs.chemmater.1c03517.